IEEE Access
Multidisciplinary ⋮ Rapid Review ⋮ Open Access Journal

Received 16 February 2023, accepted 14 March 2023, date of publication 20 March 2023, date of current version 7 April 2023.
Digital Object Identifier 10.1109/ACCESS.2023.3259219

RESEARCH ARTICLE

Novel Geometric Calibration Method for Pan-Tilt Camera With Single Control Point

JUN ZHANG[1], JIEFU WEI[1], PEI AN[2], AND XIAOMAO LIU[3]
[1]School of Artificial Intelligence and Automation, Huazhong University of Science and Technology, Wuhan 430074, China
[2]School of Electrical and Information Engineering, Wuhan Institute of Technology, Wuhan 430205, China
[3]School of Mathematics and Statistics, Huazhong University of Science and Technology, Wuhan 430074, China

Corresponding author: Pei An (anpei@wit.edu.cn)

This work was supported in part by the National Natural Science Foundation of China under Grant U1913602; and in part by the Equipment Pre-Research Project under Grant 41415020202, Grant 41415020404, and Grant 305050203.

ABSTRACT Pan-tilt (PT) camera is an indispensable part of the video surveillance systems due to its rotatable property and low cost. As the primitive output of the PT camera limits its practical applications, an accurate calibration method is required. Previous single point calibration method (SPCM) was presented to estimate angles Pan and Tilt via single control point. For the more intuitive geometric interpretation and more robust performance, we propose a novel single point calibration method (novel SPCM). In this scheme, a nonlinear PT camera function (PT function) is established via a normalization approach. With PT function, calibration problem is converted as the intersection situation of two circles formed by Pan and Tilt. Solutions can be regarded as the intersection points of two circles in 3D space. Theoretical analysis shows that novel SPCM is stable to measurement noise, for it still finds the least-square solutions even if two circles have no intersection. In the simulation experiments, reprojection error of novel SPCM is 32.4% smaller than SPCM for the large noise situation. It is 25.1% faster than SPCM. With the angle smooth strategy, novel SPCM achieves accurate and stable performance in the real data experiment.

INDEX TERMS Calibration, pan-tilt camera, control point, video surveillance.

I. INTRODUCTION

Video surveillance system has wide industrial applications in video contents analysis, objects segmentation, and visual events detection [1], [2]. Pan-tilt (PT) camera is an indispensable part of the surveillance system due to its rotatable property and low cost. In order to extract the accurate object information from the image sequence, PT camera should be calibrated with high precision in real time.

PT camera is a special type of pan-tilt-zoom (PTZ) camera without zooming. It rotates horizontally and vertically. Angles *Pan* and *Tilt* denote the horizontal and vertical angles [3], respectively. Although the platform of PT camera can measure *Pan* and *Tilt*, these measurements are not accurate enough for some industrial applications [4]. Therefore, the intrinsic and extrinsic parameters of PT camera need to be calibrated carefully. In the actual applications, some PT cameras have the small field of view (FOV) and do not cover sufficient control points, thus making it difficult for both intrinsic and extrinsic parameters estimation [5]. For PT camera, the intrinsic parameters and lens distortion coefficients are constants over frames. So, these parameters could be off-line calibrated with high precision [6]. Positions of PT camera and control points can be measured precisely by hand-hold global position systems (GPS) in advance. Therefore, only *Pan* and *Tilt* need to be calibrated in actual application.

Traditional calibration method estimates intrinsic and extrinsic parameters with at least two images or at least four control points [4], [6], [7], [8]. However, it fails to work for the extreme case that insufficient control points are found in the FOV of the camera. To deal with the extreme cases, some methods are proposed. Chen et al. [9] presented a method to estimate the focal length, *Pan*, and *Tilt* with two control points. A fast random forest method is exploited to

The associate editor coordinating the review of this manuscript and approving it for publication was Li He.

predict *Pan* and *Tilt* without image-to-image feature matching for online calibration. Li et al. [5] proposed a single point calibration method (SPCM) to estimate *Pan* and *Tilt* using only one control point in one image. *Pan* is solved with a standard quadratic equation. *Tilt* is then estimated via anti-trigonometric function. However, the geometric interpretation of SPCM is complex. And it fails to work if the quadratic equation of *Pan* has no solution.

For more intuitive geometric interpretation and more robust calibration performance, we propose a novel single point calibration method (novel SPCM). In this scheme, we exploit a vector normalization approach to establish a nonlinear PT camera function (PT function). With using PT function, calibration problem is converted as the intersection of two circles formed by *Pan* and *Tilt*, marked as $\mathbb{C}_P$ and $\mathbb{C}_T$ in 3D space, respectively. Calibration solutions are regarded as the intersection points of $\mathbb{C}_P$ and $\mathbb{C}_T$. In the extreme situation that $\mathbb{C}_P$ and $\mathbb{C}_T$ have no intersection, novel SPCM can still find the least-square solution. It means that novel SPCM is stable to large measurement noise. We also discuss the degenerated cases of novel SPCM and propose a trick to avoid them. Using PT function, our method is 25.1% faster than SPCM. Angle smooth strategy is used for the case that more than one control points are provided. Simulation experiments demonstrate that at the large noise situation, our method is 32.4% accurate than SPCM. Real-data experiments show that angle smooth strategy works for the multi-point case. Hence, we consider that novel SPCM is suitable for accurate calibration on high-speed PT cameras.

II. RELATED WORKS

PT camera is a special type of the optical camera. PT camera calibration can be referred to the general calibration methods. Most of current camera calibration methods can be classified as three categories: (i) traditional methods, (ii) self-calibration methods, and (iii) active vision methods.

Traditional method establishes the camera projection model to describe the relation of control points in world coordinate system and their corresponding 2D pixels in pixel coordinate system [6]. 3D-2D point correspondences provide constraints for intrinsic and extrinsic parameters estimation [10]. Chen et al. [9] proposed a calibration method for the PTZ camera to estimate *Pan*, *Tilt*, and the focal length using at least two control points. These parameters are refined with Levenberg-Marquardt (LM) non-linear optimization algorithm. Self-calibration method requires multi-view images registration to establish 2D-2D pixel correspondences for the intrinsic parameter estimation [7], [11], [12], [13], [14], [15], [16]. It does not need any 3D control points. Active vision method needs the camera to move at specific poses with capturing multiple images, but the camera postures and positions should be measured in high accuracy [17], [18], [19], [20], [21].

For the extreme case that camera cannot observe sufficient control points, there exist several calibration methods using only one control point [5], [22], [23]. Gatla et al. [22] estimates *Pan* and *Tilt* of industrial robot hand-eye systems using single control point in at least 60 images. Li et al. [23] proposed a method for star sensor calibration with single control point in at least 81 images. It estimates the intrinsic parameters and lens distortion coefficients via LM non-linear optimization algorithm. Li et al. [5] presented SPCM for PT camera calibration with only one control point in one image. SPCM builds a linear model with respect to *Tilt* where each element in the augmented coefficient matrix is a function of the single variable *Pan*. The closed-form solution of *Pan* is computed by solving a quadratic equation. After that, the closed-form solution of *Tilt* is obtained. Recently, based on the previous work [5], some works [9], [24] also studied the methods to calibrate the focal length and rotation matrix of PTZ camera using two control points.

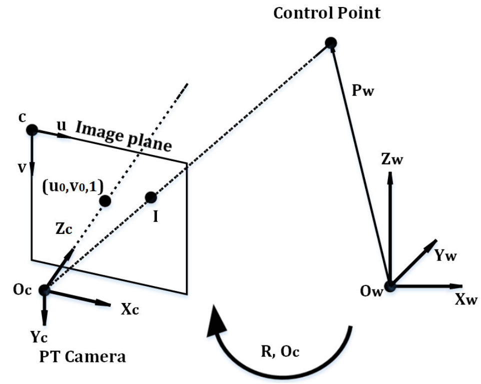

FIGURE 1. Projection model of the PT camera.

III. PT CAMERA MODEL

Parameters of PT camera include intrinsic matrix $\mathbf{K}$, lens distortion coefficients Γ, angles *Pan*, *Tilt*, and the optical center of the PT camera O_c. $\mathbf{K}$ is presented as:

$$\mathbf{K} = \begin{pmatrix} f_u & f_s & u_0 \\ 0 & f_v & v_0 \\ 0 & 0 & 1 \end{pmatrix} \tag{1}$$

where f_u and f_v denote the focal length along the u-axis and the v-axis in pixels respectively. f_s represents the skewness of the two image axes. The pixel coordinate of principle point is $(u_0, v_0, 1)^T$. In actual application, it is safe to assume that $\mathbf{K}$ and Γ of PT camera are constant [5], [9]. Thus $\mathbf{K}$ and Γ can be carefully calibrated with Zhang method [6]. O_c is measured via GPS. It means that only *Pan* and *Tilt* need to be estimated in the practical application. Distortion-free image is generated with Γ [6]. In the following analysis, pixel image coordinates are all ideal and distortion-free.

Let P_w denote the coordinates of the control point in the world coordinate system $O_w - X_wY_wZ_w$. Camera coordinate system is $O_c - X_cY_cZ_c$. I denotes the corresponding image homogeneous coordinates in the image plane $c - uv$. O_c is the optical center of PT camera in $O_w - X_wY_wZ_w$. The projection model of PT camera is presented in Fig. 1. $Z_c - axis$ is the optical axis. $X_c - axis$ and $Y_c - axis$ are parallel to the vertical and horizontal axes of the image plane, respectively. Rotation matrix $\mathbf{R}$ denotes the rotation relation of $O_w - X_wY_wZ_w$ and $O_c - X_cY_cZ_c$. Pinhole model of PT camera is presented as [6]:

$$zI = \mathbf{K} \cdot \mathbf{R}(P_w - O_c) \tag{2}$$

where z is the third element of vector $\mathbf{KR}(P_w - O_c)$. Considering that the control point is in the FOV of the camera, z in Eq. (2) must be positive. As PT camera can rotate only vertically and horizontally with embedded step motors, $\mathbf{R}$ has two degree-of-freedom. Horizontal angle is *Pan* marked as P_{gt}, and the vertical angle is *Tilt* marked as T_{gt}. They are ground truth angles. Thus, $\mathbf{R}$ can be decomposed as [5]:

$$\mathbf{R} = \mathbf{R}(X_w, -90°)\mathbf{R}(X_w, T_{gt})\mathbf{R}(Z_w, P_{gt}) \tag{3}$$

where the rotation matrix $\mathbf{R}(r, s)$ is a 3×3 rotation matrix describing rotating s angle around r axis. From the I/O ports of the platform of the PT camera, angle measures of step motors inside the platform can be obtained, and then the measurements of *Pan* and *Tilt* are computed as P_0 and T_0, which are not accurate enough. Relations between the true values and measurements are given as:

$$\begin{cases} P_{gt} = P_0 + \Delta P, \\ T_{gt} = T_0 + \Delta T, \end{cases} \tag{4}$$

where ΔP, ΔT are measurement errors of *Pan* and *Tilt*. $|\Delta P| < \varepsilon$ and $|\Delta T| < \varepsilon$. ε is the maximum angle measurement error of the platform of PT camera. In this paper, ΔP and ΔT need to be calibrated as ΔP_{est} and ΔT_{est}. With Eq. (4), angles *Pan* and *Tilt*. are estimated as P_{est} and T_{est}.

IV. CALIBRATION METHOD

In this section, we first introduce SPCM [5]. For more intuitive geometric interpretation and more robust performance, novel SPCM is proposed as presented in Fig. 2. We also analyze the degenerated case of proposed method and provide a simple trick to avoid it.

A. SPCM

We briefly introduce the calibration procedure in work [5]. Let c_θ and s_θ denote $cos(\theta)$ and $sin(\theta)$, respectively. Substituting Eqs. (3) and (4) into Eq. (2), we have

$$z\begin{pmatrix} U \\ H \\ 1 \end{pmatrix} = \begin{pmatrix} c_{\Delta P} & s_{\Delta P} & 0 \\ -s_T s_{\Delta P} & s_T c_{\Delta P} & -c_T \\ -c_T s_{\Delta P} & c_T c_{\Delta P} & s_T \end{pmatrix}\begin{pmatrix} X \\ Y \\ Z \end{pmatrix} \tag{5}$$

where

$$(U, H, 1)^T = \mathbf{K}^{-1}I$$
$$(X, Y, Z)^T = \mathbf{R}(Z, P_0)(P_w - O_c)$$

Vector product of the two sides of Eq. (5) is zero vector so that z is eliminated. After that, a linear equation of matrices related to c_T and s_T is obtained as:

$$(\mathbf{E}_{\Delta P}\ \mathbf{F}_{\Delta P})\begin{pmatrix} c_T \\ s_T \\ 1 \end{pmatrix} = \mathbf{0}_{2\times 1}$$

$$\mathbf{E}_{\Delta P} = \begin{pmatrix} UYc_{\Delta P} - UXs_{\Delta P} & ZU \\ HXs_{\Delta P} - HYc_{\Delta P} - Z & Yc_{\Delta P} - HZ - Xs_{\Delta P} \end{pmatrix}$$
$$\mathbf{F}_{\Delta P} = \begin{pmatrix} F_{11} \\ F_{12} \end{pmatrix} = \begin{pmatrix} -Xc_{\Delta P} - Ys_{\Delta P} \\ 0 \end{pmatrix} \tag{6}$$

According to Eq. (6), s_T and c_T are computed as [5]:

$$\begin{cases} c_T = -(Yc_{\Delta P} - HZ - Xs_{\Delta P}) \cdot F_{11} det(\mathbf{E}_{\Delta P})^{-1} \\ s_T = -(Z + HYc_{\Delta P} - HXs_{\Delta P}) \cdot F_{11} det(\mathbf{E}_{\Delta P})^{-1} \end{cases} \tag{7}$$

where $det(\mathbf{A})$ is the determinant of matrix $\mathbf{A}$. As $c_T^2 + s_T^2 = 1$, we obtain a standard quadratic equation of $tan(\Delta P)$, presented as:

$$a \cdot tan(\Delta P)^2 + b \cdot tan(\Delta P) + c = 0$$
$$\begin{cases} a = (H^2+1)Y^2 - U^2(X^2+Z^2), \\ b = 2XY(U^2+H^2+1), \\ c = (H^2+1)X^2 - U^2(Z^2+Y^2) \end{cases} \tag{8}$$

ΔP is solved from Eq. (8) if $\Delta = b^2 - 4ac \geq 0$ [5]. With P_0 and ΔP, P is computed via Eq. (4). Substituting ΔP into Eq. (7), T is obtained. However, the geometric interpretation in SPCM [5] is complex. Besides, SPCM has no solution of ΔP if $\Delta < 0$. It means that SPCM might not be robust to the measurement noise. Based on these facts, SPCM still needs some improvements.

B. NOVEL SPCM

For the clear geometric explanation and robust calibration performance, we proposed novel SPCM in this paper. Substituting Eqs. (3) and (4) into Eq. (2) leads to a different form unlike Eq. (5), presented as:

$$z\begin{pmatrix} U \\ V \\ W \end{pmatrix} = \mathbf{R}(X, \Delta T)\mathbf{R}(Z, \Delta P)\begin{pmatrix} X \\ Y \\ Z \end{pmatrix} \tag{9}$$

where

$$(U, V, W)^T = \mathbf{R}(X, T_0 - 90°)^T(U, H, 1)^T$$

where ΔP and ΔT need to be estimated. Let $A = (u, v, w)^T$ and $B = (x, y, z)^T$ be the normalization results of vectors $(U, V, W)^T$ and $(X, Y, Z)^T$, respectively. As $z > 0$, after the normalization of the two sides of Eq. (9), we have

$$\mathbf{R}(X, -\Delta T)A = \mathbf{R}(Z, \Delta P)B \tag{10}$$

Due to the noise disruption, Eq. (10) might not hold in the practical application. Therefore, we attempt to solve ΔP and ΔT by minimizing the following non-negative function $f(\Delta P, \Delta T)$:

$$f(\Delta P, \Delta T) = \|\mathbf{R}(X, -\Delta T)A - \mathbf{R}(Z, \Delta P)B\|_2^2$$
$$= (x_p - u)^2 + (y_p - v_t)^2 + (z - w_t)^2$$
$$(u, v_t, w_t)^T = \mathbf{R}(X, -\Delta T)A$$
$$(x_p, y_p, z)^T = \mathbf{R}(Z, \Delta P)B \tag{11}$$

As the lower bound of $f(\Delta P, \Delta T)$ is zero, ΔP and ΔT should be selected to make sure that x_p, y_p, z are closed to u, v_t, w_t, respectively. $f(\Delta P, \Delta T)$ has a core role to estimate

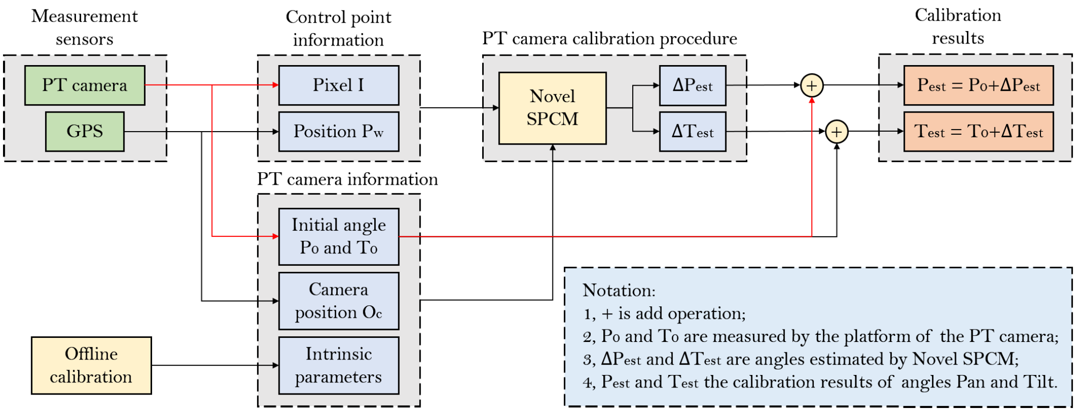

FIGURE 2. **Flowchart of proposed calibration method novel SPCM. It takes information of the i-th control point and PT camera as inputs, and estimate angles *Pan* and *Tilt* as P_{est} and T_{est}.**

ΔP and ΔT of the PT camera, thus we name it as PT function. In Eq. (11), the trajectories of $\mathbf{R}(Z, \Delta P)B$ and $\mathbf{R}(X, -\Delta T)A$ form two circles. Solutions of ΔP and ΔT are related to the intersection situations of these circles, which is discussed with detail in Sec. IV-C. As A and B are unit vectors, we have

$$x^2 + y^2 + z^2 = u^2 + v^2 + w^2 = 1$$

It can be converted as:

$$x^2 + y^2 - u^2 = v^2 + w^2 - z^2 \tag{12}$$

PT function are discussed in three cases:

1) **Case one** : $\mathbf{x^2 + y^2 - u^2 > 0}$

From Eq. (12), the condition of case one is converted as:

$$\begin{cases} x^2 + y^2 = x_p^2 + y_p^2 > u^2 \\ v^2 + w^2 = v_t^2 + w_t^2 > z^2 \end{cases} \tag{13}$$

From inequation (13), to minimize $f(\Delta P, \Delta T)$, x_p, y_p, v_t and w_t can be set as Eq. (14), in which $f(\Delta P, \Delta T)$ reaches the lower bound as zero.

$$\begin{cases} x_p = u \\ y_p = v_t = \pm(1 - u^2 - z^2)^{1/2} \\ w_t = z \end{cases} \tag{14}$$

2) **Case two** : $\mathbf{x^2 + y^2 - u^2 = 0}$

From Eq. (12), the condition of case two is converted as:

$$\begin{cases} x^2 + y^2 = x_p^2 + y_p^2 = u^2 \\ v^2 + w^2 = v_t^2 + w_t^2 = z^2 \end{cases} \tag{15}$$

From Eq. (15), to minimize $f(\Delta P, \Delta T)$,x_p, y_p, v_t and w_t can be set as Eq. (16), in which $f(\Delta P, \Delta T)$ reaches the lower bound as zero.

$$\begin{cases} x_p = u \\ y_p = v_t = 0 \\ w_t = z \end{cases} \tag{16}$$

3) **Case three** : $\mathbf{x^2 + y^2 - u^2 < 0}$

From Eq. (12), the condition of case three is converted as:

$$\begin{cases} 1 - z^2 = x^2 + y^2 = x_p^2 + y_p^2 < u^2 \Rightarrow |x_p| < |u| \\ 1 - u^2 = v^2 + w^2 = v_t^2 + w_t^2 < z^2 \Rightarrow |w_t| < |z| \end{cases} \tag{17}$$

where $x_p = u$ and $w_t = z$ cannot be established so that $f(\Delta P, \Delta T)$ cannot reach the lower bound. It means that the exact solution cannot be found from Eq. (10). Hence, we attempt to find the least-square solution of ΔP and ΔT. From inequation (17), to minimize $f(\Delta P, \Delta T)$, x_p and w_t are selected as Eq. (18) to make sure that x_p, y_p, w_t are closest to u, v_t, z, respectively.

$$\begin{cases} x_p = (1 - z^2)^{1/2} \cdot sign(u) \\ y_p = v_t = 0 \\ w_t = (1 - u^2)^{1/2} \cdot sign(z) \end{cases} \tag{18}$$

where $sign(\cdot)$ is the sign function. After obtaining x_p, y_p, v_t and w_t in above three cases, $s_{\Delta P}$, $c_{\Delta P}$, $s_{\Delta T}$ and $c_{\Delta T}$ are computed from Eqs. (19) and (20). Derivation is presented in Appendix A. After that, ΔP and ΔT can be directly calculated from these triangular functions. With P_0 and T_0, *Pan* and *Tilt* are finally estimated from Eq. (4).

$$\begin{cases} c_{\Delta P} = (x_p x + y_p y) \cdot (1 - z^2)^{-1}, \\ s_{\Delta P} = (x_p y - y_p x) \cdot (1 - z^2)^{-1}, \end{cases} \tag{19}$$

$$\begin{cases} c_{\Delta T} = (v_t v + w_t w) \cdot (1 - u^2)^{-1} \\ s_{\Delta T} = (w_t v - v_t w) \cdot (1 - u^2)^{-1} \end{cases} \tag{20}$$

According to the sign in Eq. (14), two groups of solutions exist in the first case, marked as $(\Delta P_i, \Delta T_i)(i = 1, 2)$. Under the conditions $|\Delta P| < \varepsilon$ and $|\Delta T| < \varepsilon$, we choose the solution which has smaller $|\Delta P_i| + |\Delta T_i|$.

C. GEOMETRIC INTERPRETATION OF NOVEL SPCM

Novel SPCM has been discussed with three cases in Sec. IV-B. These cases have clear geometric interpretation, presented in Fig. 3. For arbitrary ΔP and ΔT, the trajectories of $\mathbf{R}(Z, \Delta P)B$ and $\mathbf{R}(X, -\Delta T)A$ form the circles of *Pan* and *Tilt*, marked as $\mathbb{C}_P$ and $\mathbb{C}_T$. They lie on the unit sphere. Points

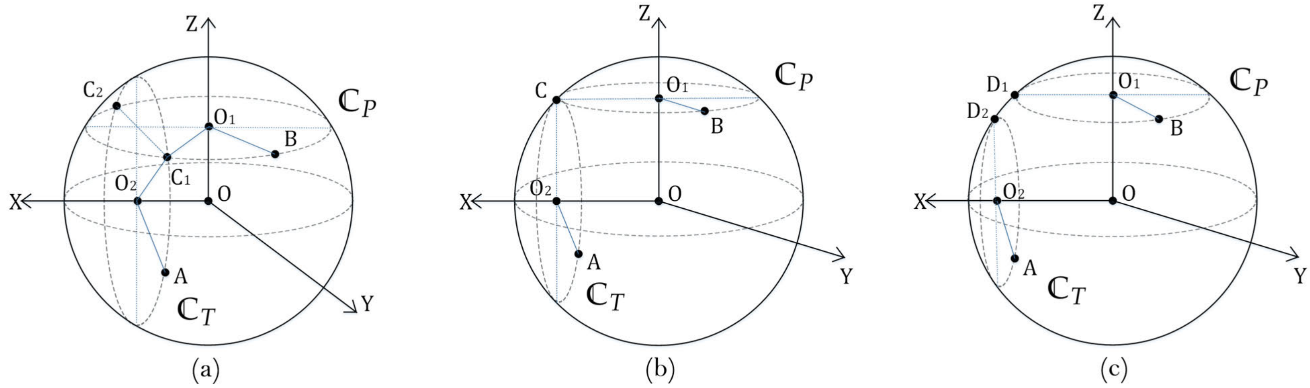

FIGURE 3. Geometric interpretation of novel SPCM in three cases. (a) Case one. (b) Case two. (c) Case three.

$O_1 = (0, 0, z)^T$ and $O_2 = (u, 0, 0)^T$ are the centers of $\mathbb{C}_P$ and $\mathbb{C}_T$. For a point p in 3D space, let p_x, p_y, and p_z denote the element of p at $X-axis$, $Y-axis$, and $Z-axis$, respectively. Geometric interpretation of novel SPCM are discussed in the following.

1) Case one : $\mathbf{x^2 + y^2 - u^2 > 0}$

According to Eq. (12), we have $x^2 + y^2 > u^2$ and $v^2 + w^2 > z^2$ in this case. Let A_x denote the element of A at X-axis. It means that the radius of $\mathbb{C}_P$ is larger than A_x, thus $\mathbb{C}_P$ and $\mathbb{C}_T$ intersect at points $C_i (i = 1, 2)$, presented in Fig. 3(a). From Eq. (14), the coordinates of points C_1 and C_2 are given in Eq. (21). As B and A can rotate to C_i, angles $\angle C_i O_1 B$ and $\angle A O_2 C_i$ represent ΔP_i and $\Delta T_i (i = 1, 2)$, respectively.

$$\begin{cases} C_1 = (u, (1 - u^2 - z^2)^{1/2}, z)^T, \\ C_2 = (u, -(1 - u^2 - z^2)^{1/2}, z)^T, \end{cases} \tag{21}$$

2) Case two : $\mathbf{x^2 + y^2 - u^2 = 0}$

According to Eq. (12), we have $x^2 + y^2 = u^2$ and $v^2 + w^2 = z^2$ in this case. It means that the radius of circle $\mathbb{C}_P$ is equal to A_x, thus circles $\mathbb{C}_P$ and $\mathbb{C}_T$ are tangent at point C, presented in Fig. 3(b). From Eq. (16), the coordinates of point C are given in Eq. (22). $\angle C O_1 B$ and $\angle A O_2 C$ represent ΔP_i and $\Delta T_i (i = 1, 2)$, respectively.

$$C = (u, 0, z)^T, \tag{22}$$

3) Case three : $\mathbf{x^2 + y^2 - u^2 < 0}$

According to Eq. (12), we have $x^2 + y^2 < u^2$ and $v^2 + w^2 < z^2$ in this case. It means that the radius of circle $\mathbb{C}_P$ is smaller than A_x, thus circles $\mathbb{C}_P$ and $\mathbb{C}_T$ do not intersect, presented in Fig. 3(c). $f(\Delta P, \Delta T)$ can be minimized if and only if ΔP and ΔT are selected to satisfy that points $\mathbf{R}(Z, \Delta P)B$ and $\mathbf{R}(X, -\Delta T)A$ coincides with points D_1 and D_2. It is discussed in Appendix B. From Eq. (18), the coordinates of points D_1, D_2 are given in Eq. (23). $\angle D_1 O_1 B$ and $\angle A O_2 D_2$ denote ΔP and ΔT, respectively.

$$\begin{cases} D_1 = ((1 - z^2)^{1/2} sign(u), 0, z)^T, \\ D_2 = (u, 0, (1 - u^2)^{1/2} sign(z))^T, \end{cases} \tag{23}$$

D. ANGLE SMOOTH STRATEGY FOR MULTI-POINT CASE

Novel SPCM can extend for the case with $N > 1$ control points. For the i-th point, angles $\Delta P(i)$ and $\Delta T(i)$ are obtained from Eqs. (19) and (20), which are not accurate enough. Angle smooth (AS) strategy is applied to optimize *Pan* and *Tilt* by minimizing the following reprojection errors:

$$E_{calib}(\Delta P, \Delta T) = \sum_{i=1}^{N} \| I(i) - I_{\text{est}}(i; \Delta P, \Delta T) \|_2^2 \tag{24}$$

where $I(i)$ is the pixel coordinates of the i-th control point. With $\Delta P(i)$ and $\Delta T(i)$, $I_{\text{est}}(i; \Delta P, \Delta T)$ is computed from Eq. (2), which is depended on ΔP and ΔT. Levenberg-Marquardt (LM) nonlinear optimization [25] is exploited to minimize Eq. (24). It requires the initial values. Initial values of ΔP, ΔT in Eq. (24) are ΔP_0, ΔT_0, presented as:

$$\Delta P_0 = \frac{1}{N} \sum_{i=1}^{N} \Delta P(i), \quad \Delta T_0 = \frac{1}{N} \sum_{i=1}^{N} \Delta T(i) \tag{25}$$

E. DEGENERATED CASE OF NOVEL SPCM

From Sec. IV-B, novel SPCM cannot work if $z^2 = 1$ or $u^2 = 1$, causing that the denominators of Eqs. (19) and (20) are zero. Two degenerated cases are discussed in the following.

1) DEGENERATED CASE ONE : $\mathbf{z^2 = 1}$

As $(x, y, z)^T$ is the normalization result of $(X, Y, Z)^T$, $z^2 = 1$ happens only if X,Y are both zero. In this case, we have

$$P_w - O_c = \mathbf{R}(Z, -P_0)(0, 0, Z)^T = (0, 0, Z)^T \tag{26}$$

It means that $P_w - O_c$ is at $Z_w - axis$, which indicates that the control point is exactly on the top or bottom of PT camera. In actual applications, we can avoid this case because it is uncommon to select the control point which is set on the top or bottom of a PT camera.

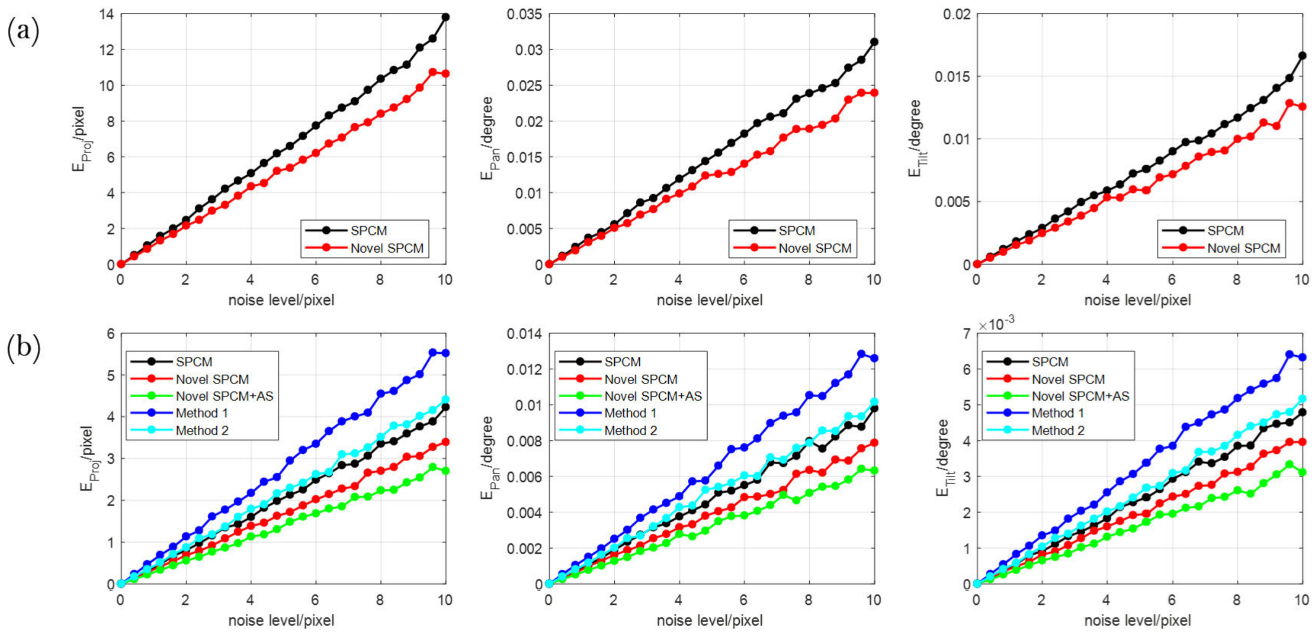

FIGURE 4. Reprojection errors, absolute errors of *Pan* and *Tilt* versus noise level. (a) Comparison results of only one control point. (b) Comparison results of ten control points with angle smooth (AS) strategy.

2) DEGENERATED CASE TWO : $\mathbf{u^2 = 1}$

As$(u, v, w)^T$ is the normalization result of $(U, V, W)^T$, $u^2 = 1$ happens only if V, W are both zero. In this case, we have

$$(U, 0, 0)^T = \mathbf{R}(X, 90^\circ - T_0)(U, 0, 0)^T = \mathbf{K}^{-1}I \tag{27}$$

From the right-hand term of Eq. (27), according to Eq. (1), it can be found that the third element of $\mathbf{K}^{-1}I$ is one. However, from the left-hand term of Eq. (27), the third element of vector $(U, 0, 0)^T$ is zero. Then Eq. (27) has contradiction so that the case $u^2 = 1$ would never happen.

F. ADVANTAGES OF NOVEL SPCM

Technically speaking, the core difference of these methods is the approaches of eliminating z in Eq. (2). Due to this difference, novel SPCM has three advantages:

(i) Novel SPCM has more intuitive geometrical interpretation, presented in Fig. 3. Solutions of ΔP and ΔT are regarded as the intersection points of $\mathbb{C}_P$ and $\mathbb{C}_T$.

(ii) Novel SPCM has more robust calibration performance, as verified in Sec. V-A2, for the normalization in Eq. (10) reduces the damage of measurement noise. For the large measurement noise, Eq. (10) might not be established strictly, meaning that $\mathbb{C}_P$ and $\mathbb{C}_T$ have no intersection. In this case, novel SPCM still has least-square solution while SPCM fails to work. It is verfied in Sec. V-A6.

(iii) Novel SPCM is more time-efficiency. From Table 1, addition and multiplication operations of novel SPCM are both less than SPCM. It is also verified in Sec. V-B3.

TABLE 1. Number of computation operations for calibration.

Method	Addition	Multiplication
Novel SPCM	42	58
SPCM [5]	47	70
Gain	11.90%	20.68%

TABLE 2. Parameters of the virtual PT camera.

Parameters	Value
$\mathrm{f_u}$/(pixels)	5600.0
$\mathrm{f_v}$/(pixels)	5600.0
$\mathrm{f_s}$/(pixels)	0.0
$\mathrm{u_0}$/(pixels)	512.0
$\mathrm{v_0}$/(pixels)	512.0
Pan/(deg)	27.4
Tilt/(deg)	58.6
$\mathrm{O_c}$/(meters)	$(1000.0, 3000.0, 5000.0)^{\mathrm{T}}$

V. EXPERIMENTS AND RESULTS

In this section, simulation and real data experiments are conducted to evaluate the performance of novel SPCM.

A. COMPUTER SIMULATIONS

1) CONFIGURATION OF EXPERIMENT

A virtual PT camera is used for simulation. Its intrinsic parameters, *Pan*, *Tilt*, and position are presented in Table 2. The size of the image plane is 1024 pixels × 1024 pixels. 125 control points block-like distributed inside the FOV are generated as the experimental dataset. In each trial, one control point is selected for parameter estimation and the rest of the control points for cross-validation. The following experiments are based on the basic configuration above. According

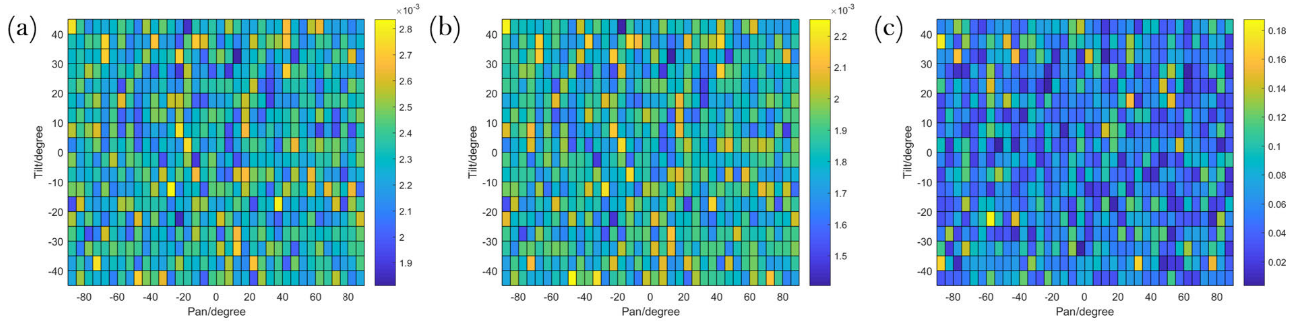

FIGURE 5. Calibration errors versus posture of PT camera.(a) Absolute error of *Pan*. (b) Absolute error of *Tilt*. (c) Reprojection error.

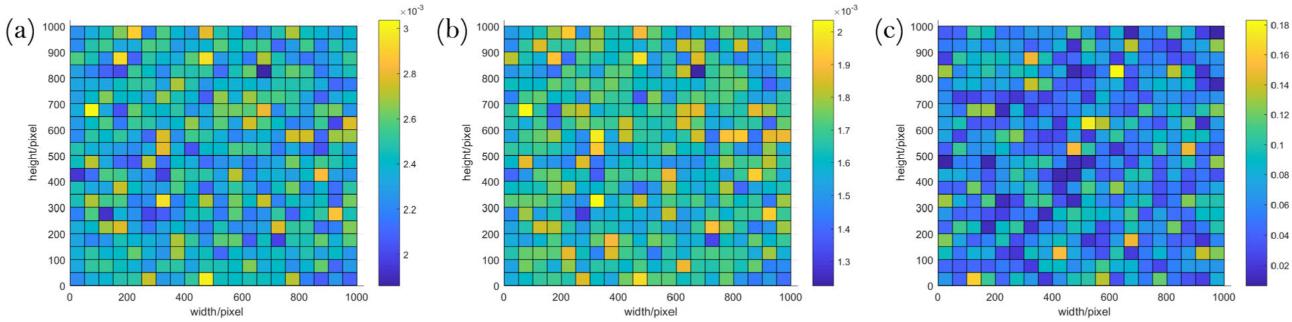

FIGURE 6. Calibration errors versus location of pixel. (a) Absolute error of *Pan*. (b) Absolute error of *Tilt*. (c) Reprojection error.

to different experimental requirements, only part of these conditions change. In the following experiments, three metrics are exploited to evaluate the calibration performance, such as absolute errors of *Pan*, *Tilt*, and the reprojection error, marked as E_{Pan}, E_{Tilt}, and E_{proj}. E_{proj} is computed via Eq. (24).

2) PERFORMANCE WITH RESPECT TO NOISE LEVEL

This experiment investigates the performance with respect to the noise level. In the practical applications, position measures of camera and control points are not accurate. Due to the image noise, pixels of control points are also not precise. Thus it is essential to test the stability of calibration method. From Eq. (2), it is noted that the position measurement errors are converted as the pixel errors. In this experiment, Gaussian noise with zero mean and σ standard deviation is added to the ground truth position of the control point in the pixel. The noise level, represented as σ, is varied from 0.0 pixels to 10.0 pixels. 500 independent trials are preformed, and the average results of our method and SPCM [5] are presented in Fig. 4. It is found that calibration error curves increase nearly linearly with fluctuation. From Fig. 4(a), calibration error of our method is smaller than SPCM. When $\sigma = 10$ pixels, reprojection error of our method is nearly 3.8 pixels ($\approx$ 32.4%) smaller than SPCM. We also test the proposed method for multi-point situation. In this case, average calibration results of all control points are used for evaluation. Current methods, such as method 1 [10] and method 2 [9], are used for comparison. From Fig. 4(b), it is found that our method outperforms SPCM and other methods. Average reprojection error is reduced by 26.4% than SPCM. With the angle smooth strategy, the calibration accuracy is also improved. It means that novel SPCM is more robust to different noise level than compared methods, for the normalization in Eq. (10) reduces the damage of pixel and position measurement noises.

3) PERFORMANCE WITH RESPECT TO THE POSTURE OF PT CAMERA

This experiment investigates the performance with respect to the posture of the PT camera. *Pan* is varied from $-90°$ to $90°$, *Tilt* from $-45°$ to $45°$. Images of simulated control points are taken under each posture of the PT camera. For each posture, 500 trials of independent noise with zero mean and standard deviation of 0.5 pixels are added. Results are presented in Fig. 5. E_{proj} fluctuates in a range smaller than 0.2 pixels. Absolute error of *Pan* and *Tilt* is smaller than 3×10^{-3} degree. Therefore, novel SPCM is available for all postures of the PT camera under the condition that the control point is in FOV of the PT camera.

4) PERFORMANCE WITH RESPECT TO LOCATION OF PIXEL

This experiment investigates the performance regarding the location of pixel in the image plane. As the size of the stimulative image plane is 1024 pixels $\times$ 1024 pixels. We obtain 10^4 pixel points in total and sample at 10 pixels interval. For each posture, 500 trials of independent noise with zero mean and standard deviation of 0.5 pixels are added. From Fig. 6, it is found that E_{proj} is less than 0.2 pixels. Average of E_{proj}

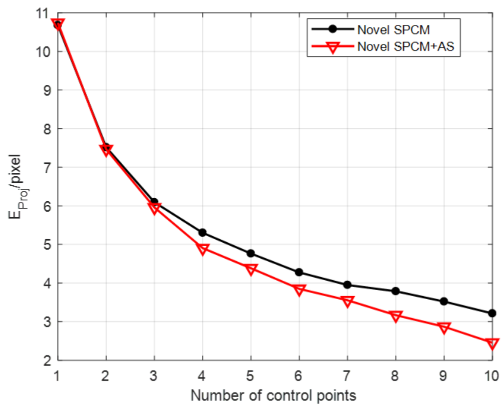

FIGURE 7. Calibration performance of angle smooth strategy.

TABLE 3. Comparison results in the extreme calibration case.

Method	E_{proj}/pixel	E_{Tilt}/deg	E_{Pan}/deg
SPCM [5]	19.73	0.27	0.33
Novel SPCM	6.47	0.016	0.0097

is 0.0082 pixels. Absolute error of *Pan* and *Tilt* is smaller than 5×10^{-3} degree. Hence, novel SPCM is available for the whole image plane.

5) PERFORMANCE WITH RESPECT TO ANGLE SMOOTH STRATEGY

This experiment investigates the performance regarding the angle smooth strategy. Number of control points N ranges from 1 to 10. Pixel noise with $\sigma = 10$ pixels is added. Reprojection errors are presented in Fig. 7. With N increasing, the calibration performance with angle smooth strategy is more accurate, for the optimization in Eq. (24) is robust to noise.

6) PERFORMANCE WITH RESPECT TO THE EXTREME SITUATION

This experiment investigates the performance regarding the extreme situation. Pixel and position errors are added to the pixel and position of the control point, to satisfy the case three in Sec. IV-B. In this situation, $\mathbb{C}_P$ and $\mathbb{C}_T$ do not intersect, and ΔP in Eq. (8) is negative. For SPCM [5], ΔP and ΔT cannot be solved, and have to set as zero. While our method can still compute ΔP and ΔT via Eqs. (18)-(20). Reprojection errors are presented in Table 3. It is found that our method is more stable in the extreme calibration case.

B. REAL DATA EXPERIMENTS

1) CONFIGURATION OF EXPERIMENT

Industrial PT camera is exploited in the real data experiment. Its intrinsic parameters and distortion coefficients have been calibrated by method [6] in advance. With lens distortion coefficients, distortion-free image is generated [6]. Thus pixel image coordinates are all ideal and distortion-free. Intrinsic parameters of PT camera are presented in Table 4. From the I/O port of the platform of PT camera, P_0 and T_0 are measured as 178° and −10°, respectively. The size of the image plane is 1024 pixels × 1024 pixels. In this experiment, ten control points are fallen into the FOV of PT camera. Positions of control points and PT camera are presented in Table 5 measured by a hand-hold GPS in high precision. In this experiment, raw GPS measures are first converted to WGS-84 (World Geodetic System-1984 Coordinate System) coordinates, and then converted to the coordinates in the local geodetic coordinate system. In the following experiments, the local geodetic coordinate system is considered as the world coordinate system. It is noted that O_c cannot be measured directly. In this paper, O_c is estimated by measuring the position of camera lens, with the prior information of camera size. Measurement errors of optical center and control points are existed for all compared methods. Ground truths of *Pan* and *Tilt* are unknown. Thus, reprojection error is used to evaluate the calibration performance.

TABLE 4. Parameters of PT camera in real data experiment.

Parameters	Value
f_u/(pixels)	2925.732
f_v/(pixels)	2962.458
f_s/(pixels)	1.237
u_0/(pixels)	511.905
v_0/(pixels)	512.021
P_0/(deg)	178.0
T_0/(deg)	−10.0

TABLE 5. Positions of control points and PT camera. X-axis, Y-axis, and Z-axis denote the coordinate of the control point at the corresponding axis in $O_W - X_W Y_W Z_W$ (Unit: meters). u-axis and v-axis denote the coordinate of the control point at the corresponding axis in the image coordinate system (Unit: pixels). O_c is the position of PT camera.

Point	X-axis	Y-axis	Z-axis	u-axis	v-axis
O_c	251142.67	3379632.89	86.1	–	–
1	251144.11	3379608.60	79.5	263.6	751.2
2	251138.03	3379608.28	79.4	964.3	747.8
3	251137.81	3379607.88	81.6	988.1	482.5
4	251139.71	3379606.14	82.5	751.7	359.3
5	251141.56	3379606.02	82.9	550.2	314.6
6	251142.14	3379604.93	83.2	485.4	266.5
7	251144.52	3379604.85	83.3	235.7	258.2
8	251144.23	3379605.93	83.0	260.1	303.2
9	251145.72	3379604.80	83.4	111.8	250.4
10	251145.92	3379607.94	80.0	59.9	671.3

2) MODEL COMPARISONS

Calibration method is applied to the dataset on Table 5, to estimate *Pan* and *Tilt*. Compared with novel SPCM, SPCM [5], method 1 [10] and method 2 [9] are selected for model comparisons. Although different methods require different numbers of points, ten control points satisfy all requirements. In SPCM, ten control points are used in turn for angles estimation and the average value is taken as the final calibration result. With more than one control points, angle smooth strategy is exploited for novel SPCM. In methods 1 and 2, ten control points are used together for parameter estimation in one trial. For method 1, ten control points can be used to compute

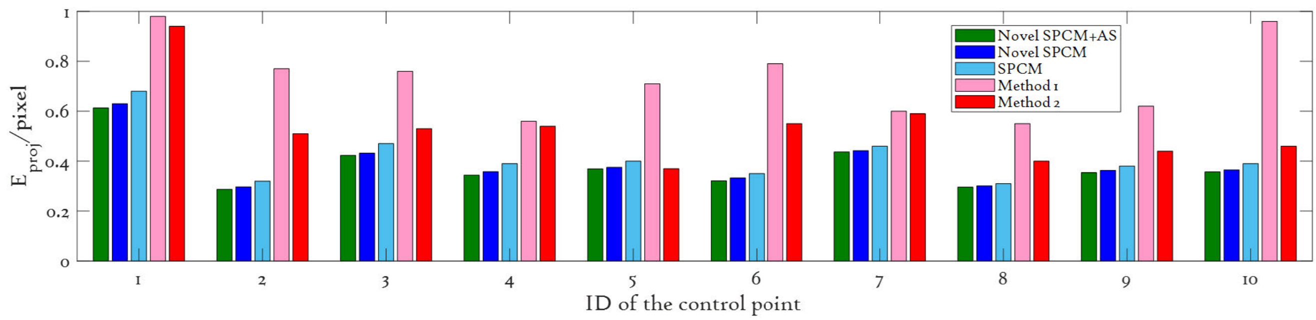

FIGURE 8. Reprojection errors of different methods in real data experiment. AS denotes the angle smooth strategy.

the least-square solution of the projection matrix of the PT camera via direct linear transformation (DLT) method [10]. In method 2, ten control points are used to compute *Pan*, *Tilt* and the focal length using the LM non-linear minimization algorithm. In each trial, Reprojection error are measured between the actual pixel values of test point and its estimated pixel value. Comparison results are presented in Fig. 8. The horizontal axis is the ID of the control point and the vertical axis is reprojection error of the corresponding control point. The green bars denote the results of Novel SPCM with angle smooth strategy; the deep blue bars denote the results of novel SPCM; the light blue bars denote the results of SPCM; the pink bars denote the results of method 1; the yellow bars denote the results of method 2; the red bars denote the results without using any calibration methods. It is found that novel SPCM has smaller reprojection errors than SPCM [5] for all control points, especially for the first and third control points. The reason has been discussed in Sec. V-A2. From Fig. 8, Novel SPCM and SPCM are both superior to other methods and the initial output results. Novel SPCM is better in accuracy because method 1 estimates the 3×4 projection matrix without using the known information, such as the intrinsic parameters of the PT camera. Method 2 assumes that f_s is zero and $f_u = f_v$, which may not be true in the actual application. It is also found that angle smooth strategy can improve the accuracy of calibration when more than one control points are provided. With angle smooth strategy, mean RMS error of our method is 0.380 pixels, 9.21% and 6.68% smaller than SPCM and novel SPCM. Therefore, with angle smooth strategy, our method is superior to current methods for the case with more than one control point.

3) TIME CONSUMING TEST

For further comparison of novel SPCM and SPCM [5], we design an experiment for time-consuming test. Novel SPCM and SPCM are both implemented with MATLAB 2017*a* on an Intel $i7 - 4810MQ$ 2.80GHz CPU, 16.0GB memory Windows 2012 64-bit operating system. With the same information of the control points and the PT camera provided in Tables 4 and 5, 500 independent trials are performed, and the average times of these methods are computed. Results are presented in Table 6. The operation time of novel SPCM is decreased by nearly 25.1% than SPCM, which is verified the conclusion in Sec. IV-F. Therefore, novel SPCM is suitable for calibrating high-speed PT camera.

TABLE 6. Results of time-consuming test.

Method	Novel SPCM	SPCM [5]	Gain
Times/($\times 10^{-6}$s)	3.46	4.33	25.1%

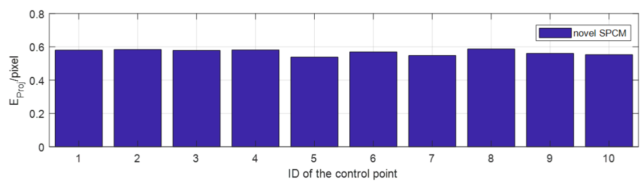

FIGURE 9. RMS errors of cross-validation in real data experiment.

4) CROSS-VALIDATION

In order to further study the stability of novel SPCM, it is applied to the dataset on Table 5 to do cross-validation. Each of the ten control points is used in turn for parameter estimation and the remaining nine control points as the test points for cross-validation. In each trial, we compute the RMS error between the actual pixel values of the test points and its estimated pixel values, and then calculate the average of the errors of nine test points to get the final result. Results are presented in Fig. 9. The mean and deviation of novel SPCM are 0.5699 pixels and 1.68×10^{-4} pixels, respectively. Small deviation and average means that novel SPCM is stable.

VI. CONCLUSION

We propose novel SPCM as an improvement of SPCM [5]. In this scheme, with PT function, calibration problem is converted as the intersection situation of two circles $\mathbb{C}_P$ and $\mathbb{C}_T$. ΔP and ΔT are regarded as the intersection points of $\mathbb{C}_P$ and $\mathbb{C}_T$. Simulations demonstrate that our method is 32.4% accurate than SPCM at the noise situation with $\sigma = 10$ pixels. Our method is also 25.1% faster than SPCM. Therefore, we believe that the proposed method contributes to the industrial camera calibration.

APPENDIX

A. DERIVATIONS OF EQS. (19) AND (20)

$(u, v_t, w_t)^T = \mathbf{R}(X, -\Delta T)A$ and $(x_p, y_p, z)^T = \mathbf{R}(Z, \Delta P)B$ can be converted as:

$$\begin{pmatrix} x_p \\ y_p \end{pmatrix} = \begin{pmatrix} c_{\Delta P} & s_{\Delta P} \\ -s_{\Delta P} & c_{\Delta P} \end{pmatrix} \begin{pmatrix} x \\ y \end{pmatrix} \tag{28}$$

$$\begin{pmatrix} v_t \\ w_t \end{pmatrix} = \begin{pmatrix} c_{\Delta T} & -s_{\Delta T} \\ s_{\Delta T} & c_{\Delta T} \end{pmatrix} \begin{pmatrix} v \\ w \end{pmatrix} \tag{29}$$

Eq. (28) can be transformed as the linear equation of two unknowns related to $c_{\Delta P}, s_{\Delta P}$. $c_{\Delta P}$ and $s_{\Delta P}$ are solved as Eq. (19). Eq. (29) is also converted as the linear equation related to $c_{\Delta T}, s_{\Delta T}$. $c_{\Delta T}$ and $s_{\Delta T}$ are solved as Eq. (20).

B. ILLUSTRATION OF POINTS D_1 AND D_2 IN CASE THREE

The coordinates of points E_1, E_2, as presented in Fig. 10, are $\mathbf{R}(Z, \Delta P)B$ and $\mathbf{R}(X, -\Delta T)A$, respectively. For arbitrary angles ΔP and ΔT, the trajectories of E_1, E_2 form two circles $\mathbb{C}_P$ (on plane 1) and $\mathbb{C}_T$ (on plane 2). The geometric interpretation of minimizing $f(\Delta P, \Delta T)$ is to find parameters ΔP and ΔT to minimize the distance between E_1 and E_2.

The coordinates of points D_1 and D_2 are shown as:

$$\begin{cases} D_1 = ((1 - z^2)^{1/2} sign(u), 0, z)^T, \\ D_2 = (u, 0, (1 - u^2)^{1/2} sign(z))^T, \end{cases} \tag{30}$$

We would illustrate that compared with the distance between any points E_1 and E_2,where E_1 is a point on the circle $\mathbb{C}_P$, E_2 is a point on the circle $\mathbb{C}_T$, the distance between points D_1 and D_2 is the shortest, which means inequation (31) is always right.

$$|D_1D_2| \leq |E_1E_2| \tag{31}$$

From Fig. 10, it is found that line L is the intersection of the plane 1 and plane 2 while plane 1 is perpendicular to plane 2. Point D_3 lies on line L and the line segment D_1D_3 is perpendicular to D_2D_3. Points E_3 and E_4 both lie on line L. Line segment E_2E_3 is perpendicular to plane 1. And line segment E_1E_4 is perpendicular to the plane 2. After that, we have,

$$|D_1D_2|^2 = |D_1D_3|^2 + |D_2D_3|^2 \leq |E_4E_1|^2 + |E_2E_3|^2 \tag{32}$$

As $|E_3E_4|^2 \geq 0$, it can be converted as:

$$|D_1D_2|^2 \leq |E_4E_1|^2 + |E_2E_3|^2 + |E_3E_4|^2 = |E_1E_2|^2 \tag{33}$$

Finally, the inequation (31) is obtained.

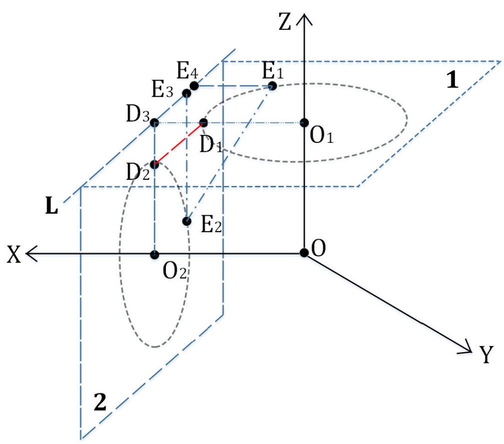

FIGURE 10. Geometric interpretations in case three.

ACKNOWLEDGMENT

The authors would like to thank Siying Ke, Dr. Daimeng Zhang, and Dr. Dakang Ma for providing suggestions.

REFERENCES

[1] D. K. Yadav, L. Sharma, and S. K. Bharti, "Moving object detection in real-time visual surveillance using background subtraction technique," in *Proc. 14th Int. Conf. Hybrid Intell. Syst.*, Dec. 2014, pp. 79–84.

[2] S. C. Lee and R. Nevatia, "Hierarchical abnormal event detection by real time and semi-real time multi-tasking video surveillance system," *Mach. Vis. Appl.*, vol. 25, no. 1, pp. 133–143, 2014.

[3] J. Davis and X. Chen, "Calibrating pan-tilt cameras in wide-area surveillance networks," in *Proc. 9th IEEE Int. Conf. Comput. Vis.*, Oct. 2003, pp. 144–149.

[4] F. Rameau, A. Habed, C. Demonceaux, D. Sidibe, and D. Fofi, "Self-calibration of a PTZ camera using new LMI constraints," in *Proc. Asian Conf. Comput. Vis.*, 2012, pp. 297–308.

[5] Y. Li, J. Zhang, and J. Tian, "Method for pan-tilt camera calibration using single control point," *J. Opt. Soc. Amer. A, Opt. Image Sci.*, vol. 32, no. 1, pp. 156–163, 2015.

[6] Z. Zhang, "A flexible new technique for camera calibration," *IEEE Trans. Pattern Anal. Mach. Intell.*, vol. 22, no. 11, pp. 1330–1334, Nov. 2000.

[7] I. N. Junejo and H. Foroosh, "Refining PTZ camera calibration," in *Proc. 19th Int. Conf. Pattern Recognit.*, Dec. 2008, pp. 1–4.

[8] Z. Wu and R. J. Radke, "Keeping a pan-tilt-zoom camera calibrated," *IEEE Trans. Pattern Anal. Mach. Intell.*, vol. 35, no. 8, pp. 1994–2007, Aug. 2013.

[9] J. Chen, F. Zhu, and J. J. Little, "A two-point method for PTZ camera calibration in sports," in *Proc. IEEE Winter Conf. Appl. Comput. Vis. (WACV)*, Mar. 2018, pp. 287–295.

[10] Y. I. Abdel-Aziz and H. M. Karara, "Direct linear transformation into object shape coordinates in close-range photogrammetry," in *Proc. Symp. Close-Range Photogramm.*, 1971, pp. 1–18.

[11] G.-Q. Wei and S. D. Ma, "Two plane camera calibration: A unified model," in *Proc. IEEE Comput. Soc. Conf. Comput. Vis. Pattern Recognit.*, Jan. 1991, pp. 133–138.

[12] L. N. Smith and M. L. Smith, "Automatic machine vision calibration using statistical and neural network methods," *Image Vis. Comput.*, vol. 23, no. 10, pp. 887–899, Sep. 2005.

[13] O. D. Faugeras, Q. Luong, and S. J. Maybank, "Camera self-calibration: Theory and experiments," in *Proc. Eur. Conf. Comput. Vis.*, 1992, pp. 321–334.

[14] A. W. K. Tang and Y. S. Hung, "A self-calibration algorithm based on a unified framework for constraints on multiple views," *J. Math. Imag. Vis.*, vol. 44, no. 3, pp. 432–448, Nov. 2012.

[15] A. Basu and K. Ravi, "Active camera calibration using pan, tilt and roll," *IEEE Trans. Syst., Man, Cybern., B*, vol. 27, no. 3, pp. 559–566, Jun. 1997.

[16] S. Álvarez, D. F. Llorca, and M. A. Sotelo, "Hierarchical camera auto-calibration for traffic surveillance systems," *Exp. Syst. Appl.*, vol. 41, no. 4, pp. 1532–1542, Mar. 2014.

[17] R. I. Hartley, "Self-calibration of stationary cameras," *Int. J. Comput. Vis.*, vol. 22, no. 1, pp. 5–23, Feb. 1997.

[18] R. I. Hartley, "Self-calibration from multiple views with a rotating camera," in *Proc. Eur. Conf. Comput. Vis.*, 1994, pp. 471–478.

[19] J. Knight, A. Zisserman, and I. Reid, "Linear auto-calibration for ground plane motion," in *Proc. IEEE Comput. Soc. Conf. Comput. Vis. Pattern Recognit.*, Jul. 2003, pp. 503–510.

[20] S. De Ma, "A self-calibration technique for active vision systems," *IEEE Trans. Robot. Autom.* vol. 12, no. 1, pp. 114–120, Feb. 1996.

[21] J. Komorowski and P. Rokita, "Extrinsic camera calibration method and its performance evaluation," in *Proc. Int. Conf. Comput. Vis. Graph.*, 2012, pp. 129–138.
[22] C. S. Gatla, R. Lumia, J. Wood, and G. Starr, "Calibrating pan-tilt cameras in robot hand-eye systems using a single point," in *Proc. IEEE Int. Conf. Robot. Autom.*, Apr. 2007, pp. 3186–3191.
[23] Y. Li, J. Zhang, W. Hu, and J. Tian, "Laboratory calibration of star sensor with installation error using a nonlinear distortion model," *Appl. Phys. B, Lasers Opt.*, vol. 115, no. 4, pp. 561–570, 2013.
[24] P. An, J. Ma, T. Ma, B. Fang, Y. Kun, X. Liu, and J. Zhang, "Two-point calibration method for a zoom camera with an approximate focal-invariant radial distortion model," *J. Opt. Soc. Amer. A, Opt. Image Sci.*, vol. 38, no. 4, pp. 504–514, 2021.
[25] J. More, "The Levenberg–Marquardt algorithm, implementation and theory," *Numer. Anal.*, vol. 630, no. 1, pp. 105–116, 1977.

JUN ZHANG received the Ph.D. degree from the Huazhong University of Science and Technology, Wuhan, China, in 2006. He is currently an Associate Professor with the School of Artificial Intelligence and Automation, Huazhong University of Science and Technology. His research interests include camera calibration, image process, pattern recognition, and machine learning.

JIEFU WEI is currently pursuing the master's degree with the Huazhong University of Science and Technology. His research interests include camera calibration and image process.

PEI AN received the Ph.D. degree from the Huazhong University of Science and Technology, in 2022. He is currently a Lecturer with the Wuhan Institute of Technology. His current research interests include 3D object detection, semi-supervised learning, and LiDAR simulation.

XIAOMAO LIU received the Ph.D. degree from the Huazhong University of Science and Technology, Wuhan, China, in 2001. She is currently an Associate Professor with the School of Mathematics and Statistics, Huazhong University of Science and Technology. Her research interests include statistics, pattern recognition, and machine learning.